Supporting Information

Munro et al. 10.1073/pnas.0908597107

SI Text

SI Materials and Methods. ***Preparation and activity of fluorescently labeled ribosome complexes.*** Ribosomal protein L1 was cloned into the pET-SUMO vector (Invitrogen) for overexpression and purification by nickel chromatography. The S55C mutation was made by site-directed mutagenesis (Stratagene). L1 was labeled with Cy5- of Cy5.5-maleimide (GE Healthcare) as described (14). $tRNA^{Phe}$(Cy3-s^4U8) was aminoacylated in a reaction of 2 μM $tRNA^{Phe}$(Cy3-s^4U8), 2 μM phenylalanyl tRNA synthetase, 4 μM EF-Tu, 3 μg/mL myokinase, and 30 μg/mL pyruvate kinase, in a buffer containing 25 mM Tris-OAc pH 8.5, 40 mM $Mg(OAc)_2$, 20% DMSO, 1 mM DTT, 40 μM phenylalanine, 400 μM GTP, 500 μM ATP, and 800 μM phosphoenolpyruvate. The reaction was then phenol-extracted and N-acetylated through incubation with 0.1% acetic anhydride for 1 hour on ice, followed by ethanol precipitation.

The activity of ribosome complexes containing L1(Cy5-S55C) was first verified by a single-molecule fluorescence-based puromycin assay that reports on the incremental steps of tRNA selection, hybrid state formation, and translocation (2, 6). Puromycin, an analogue of the 3′ aminoacyl terminus of tRNA, reacts with peptidyl-tRNA located at the P site, releasing the peptide chain from the ribosome. Puromycin reactivity can therefore be readily tracked by dye-labeling the peptide (2). Complexes with an empty A site react rapidly. tRNA occupancy in the A site greatly reduces puromycin reactivity by competitively inhibiting puromycin binding; residual reactivity reflects transient excursions of its 3′ end to the large subunit P site (2, 10, 11). Translocation, by vacating the A site, leads to the recovery of rapid puromycin reactivity. Puromycin reactivity profiles of 70S ribosome complexes lacking L1 show a specific defect in pretranslocation puromycin reactivity (Fig. S3) consistent with reduced occupancy of puromycin-reactive hybrid states (6). The reconstitution of wild-type L1 into L1-depleted ribosomes specifically recovered this defect; reconstitution of L1(Cy5-S55C) into L1-depleted ribosomes recovered the puromycin reactivity to an extent consistent with ~90% incorporation of the labeled protein.

A fluorescence based kinetic assay (1) was used to measure the rates of translocation on wild-type, ΔL1, and L1-reconstituted ribosomes. Ribosomes were initiated on a pyrene-labeled gene-32 derived mRNA as described in *Materials and Methods.* The A site was filled enzymatically by addition of 2 μM EF-Tu(GTP)-aa-tRNA, prepared as previously described (6, 15), to 1 μM initiation complex and incubated for 2 min at 37 °C. Translation factors and unbound tRNA were removed by sucrose-cushion ultracentrifugation in Tris Polymix buffer with 20 mM $Mg(OAc)_2$. Upon translocation, pyrene fluorescence is quenched due to interactions with the ribosomal A site. Rapid stopped-flow mixing of 10 μM EF-G and 1 mM GTP with 0.2 μM pretranslocation ribosomes and the subsequent loss of fluorescence were monitored with a SX20 stopped-flow instrument (Applied Photophysics) affixed with a 375-nm long-pass emission filter (Schott). Each experiment was repeated 5–7 times, and the resulting fluorescence decay traces were analyzed as described below. All experiments were performed in Tris Polymix buffer with 15 mM $Mg(OAc)_2$ at 25 °C.

Analysis of bulk translocation data. The time-resolved decay in fluorescence due to translocation of a pyrene-labeled mRNA was measured with a SX20 stopped-flow fluorimeter (Applied Photophysics). The data were analyzed by fitting each individual fluorescence trace to the double exponential function $A_1e^{-k_1t} + A_2e^{-k_2t} + y_0$ in Origin, resulting in fits with $R^2 > 0.9$. The dominant (fast) rates from 3-7 measurements were averaged and reported in Table S1 along with standard errors.

Acquisition of smFRET data. In all experiments, the Cy3 fluorophore was excited at ~0.5 kW/cm^2 (Laser Quantum, 532 nm). In two-color smFRET experiments, fluorescence from Cy3 and Cy5 were separated by a 650DCXR dichroic filter and imaged on a Cascade 128 CCD camera (Photometrics) at 40-ms time resolution. In three-color smFRET experiments, fluorescence from Cy3, Cy5, and Cy5.5 were separated with 630DCXR and 690DCLP dichroic filters. The Cy3, Cy5, and Cy5.5 channels were then filtered with HQ580/60m, HQ670/40m, and HQ725/50m bandpass filters, respectively, and imaged on a Cascade 512B CCD camera at 40-ms time resolution (Photometrics). All filters were purchased from Chroma. Single-molecule fluorescence traces were extracted from the movies in Matlab (Mathworks). Two-color FRET efficiency was calculated according to FRET $= I_{Cy5}/(I_{Cy3} + I_{Cy5})$. Three-color FRET efficiencies were calculated according to Cy5 FRET $= I_{Cy5}/(I_{Cy3} + I_{Cy5} + I_{Cy5.5})$, and Cy5.5 FRET $= I_{Cy5.5}/(I_{Cy3} + I_{Cy5} + I_{Cy5.5})$.

Kinetic analysis of smFRET data. Single-molecule fluorescence trajectories were extracted from the movies by using custom-made programs in Matlab (Mathworks). To eliminate user bias and increase throughput, trajectories fit for kinetic analysis were identified according to a fully automated protocol implemented in Matlab. Trajectories were selected according to six criteria: (*i*) minimum total intensity (combined Cy3 and Cy5 fluorescence intensity) threshold of 7,000 arbitrary units (a.u.); (*ii*) maximum total intensity of 25,000 a.u.; (*iii*) minimum signal-to-noise ratio of 8, defined as the signal magnitude divided by the standard deviation of the background intensity after photobleaching; (*iv*) maximum standard deviation of the background intensity of 1,500 a.u.; (*v*) a single detected photobleaching event; (*vi*) minimum FRET lifetime of 5 frames.

The rates of transition between FRET states were established by first idealizing the trajectories to Markov chain models using the segmental k-means algorithm implemented in QuB (5). The procedure for model selection for data acquired on complexes bearing labeled L1 and P-site tRNA is described in the following section and in Figs. S4 and S5; the model for analysis of trajectories acquired on complexes with two labeled tRNAs was previously determined (6). The distributions of data points assigned to each FRET state were then formed by using the idealization (Figs. 2 and 3); zero-FRET state distributions were disregarded so that the low-FRET state could be more clearly visualized. The idealization was then used to optimize the model parameters by maximum likelihood optimization in QuB (7). The trajectories were analyzed separately such that one set of rate constants was estimated for each trace. Each dataset was then randomly split into three subsets to be analyzed in parallel. Under the assumption of homogeneous broadening in free energy, the rate constants for each transition from all trajectories were log-transformed, and the resulting symmetric distribution was fit to a Gaussian (16). The rate constant for each transition was recovered by exponentiation of the distribution mean. As described below, these rates were used to calculate the summary rates reported in Table 1. The results of the analyses of the three subsets were averaged, and reported in Tables 1 and S2 along with standard errors.

Model selection. Upon visual inspection of the filtered smFRET trajectories acquired from complexes with L1(Cy5-S55C) and labeled P-site $tRNA^{fMet}$ or $tRNA^{Phe}$, a low-FRET (~0.1) state and a high-FRET state (~0.65) were readily identified. Intermediate-FRET states (~0.25 and ~0.4) were also seen (Figs. S4 and S5), but their existence warranted quantitative confirmation. To verify the existence of the intermediate states, the smFRET trajectories were idealized to four different models by using the segmental k-means algorithm implemented in QuB (5). The two-, three-, and four-state models used for idealization are shown in Fig. S4. A five-state model was also considered in which a 0.5-FRET state was added to the four-state model. The five-state model was considered only as a means of testing the robustness of the following model selection procedure. To identify which model best represented the smFRET trajectories, the Akaike information criterion (AIC) was calculated for each idealization (12). By assuming that the errors in idealization are distributed normally, AIC may be taken as

$$\mathrm{AIC} = \ln \sigma^2 + \frac{2(k+1)}{n},$$

where n is the number of data points idealized, k is the number of rate constants in the model, and

$$\sigma^2 = \frac{1}{n}\sum_{i=1}^{n}(x_i - \bar{x}_i)^2,$$

where x_i is the data point which has been idealized and $\bar{x}_i$ is the value of the FRET state that has been assigned to x_i (17). The AIC values obtained from each of the four idealizations are shown in Fig. S4*D*. A decrease in AIC is seen upon addition of a single intermediate state (0.25 FRET), indicating that the two-state model does not provide the best representation of the data. A further decrease in AIC is seen upon addition of the 0.4-FRET state. Inclusion of the fifth state resulted in an increase in the AIC. Having resulted in the minimum of the AIC, the four-state model was selected for further kinetic analysis.

Visual inspection of the smFRET trajectories, and the TDPs shown in Fig. S4, Fig. S5 indicated the existence of transitions directly between the 0.1 and 0.4 FRET states and between 0.1 and 0.65 FRET. Both of these transitions could occur by way of at least one intermediate dwell that was too short to be detected at the current time resolution of 40 ms. To assess the possibility that transitions between 0.1 and 0.4 FRET and between 0.1 and 0.65 FRET are due to missed dwells in intermediate states, FRET trajectories were generated by Monte Carlo simulation from the four-state linear model, which does not explicitly allow transitions directly from 0.1 to 0.4 or 0.65 FRET. In both the experimental and the simulated trajectories, the number of transitions to 0.4 and 0.65 FRET that occurred by way of intermediate states was compared to the number of transitions directly from 0.1 to 0.4 or 0.65 FRET. In both the experimental and the simulated trajectories, ~49% of the transitions between 0.1 and 0.65 FRET occurred with no detected dwell in the intermediate FRET states. This finding indicated that virtually all of the transitions directly between 0.1 and 0.65 FRET can be accounted for my missed dwells in the 0.25 and 0.4 FRET states. In the case of transitions between 0.1 and 0.4 FRET, the simulated trajectories showed that ~40% of these transitions occur with no intermediate dwell in 0.25 FRET, as compared to ~69% in the experimental data. Taken together, these observations indicated that no direct connection is needed between 0.1 and 0.65 FRET but that a connection between 0.1 and 0.4 FRET might improve the fit of the four-state model (Fig. S4).

The rates of interconversion between the four FRET states in the linear and looped models were determined through a maximum likelihood optimization procedure implemented in QuB (7, 18), with a dead time of 30 ms. A loop balance constraint was imposed during optimization of the looped model. To assess the relative fitness of the four-state linear and looped models, the maximized log-likelihoods per transition were compared. The log-likelihoods per transition were adjusted for the different number of model parameters in the two models by using the AIC,

$$\mathrm{AIC} = 2k - 2\ell,$$

where ℓ is the log-likelihood per transition summed over all trajectories and k is the number of adjustable parameters in the model (12): $k = 6$ for the linear model and 8 for the looped model. Fig. S4 clearly shows a decrease in AIC upon addition of the connection between the 0.1 and 0.4 FRET states, indicating that the four-state looped model represents the data better than the linear model. Therefore, the four-state looped model was used to estimate the rates of interconversion between the observed FRET states shown in Tables 1 and Table S2.

Calculation of rates of transition out of aggregated FRET states. Estimation of the rate of transition into the high-FRET state ($k_{\to\mathrm{high}}$) requires calculation of the aggregate lifetime of the 0.1, 0.25, and 0.4 FRET states, which are all in dynamic exchange. Likewise, calculation of the rate of transition into the low-FRET state ($k_{\to\mathrm{low}}$) requires the aggregate lifetime of the 0.25, 0.4, and 0.65 FRET states. These rates were calculated according to the method of Colquhoun and Hawkes (19), which is outlined here. In the case of the rate of transition into high FRET, we require the conditional probability density of transition from the 0.1, 0.25, or 0.4 FRET states into 0.65 FRET:

$$f(t) = w_1 \exp(-\kappa_1 t) + w_2 \exp(-\kappa_2 t) + w_3 \exp(-\kappa_3 t).$$

The rate of transition out of these states can then be determined from

$$\frac{1}{k_{\to\mathrm{high}}} \equiv \langle t \rangle = \int_0^\infty t f(t) dt,$$

$$k_{\to\mathrm{high}} = \frac{\kappa_1^2\kappa_2^2\kappa_3^2}{w_1\kappa_2^2\kappa_3^2 + w_2\kappa_1^2\kappa_3^2 + w_3\kappa_1^2\kappa_2^2}.$$

We therefore need only the weighting factors w_i and the associated time constants κ_i. These may be determined from the master equation describing the transition probabilities $P_{i\to 4}$, where i is 1, 2, 3, or 4, corresponding to 0.1, 0.25, 0.4, or 0.65 FRET, respectively:

$$\frac{dP_{i\to 4}(t)}{dt} = P_{i\to 1}(t)k_{1\to 4} + P_{i\to 2}(t)k_{2\to 4} + P_{i\to 3}(t)k_{3\to 4}.$$

We can then reexpress the probability density $f(t)$ as

$$f(t) = \pi_1 \frac{dP_{1\to 4}(t)}{dt} + \pi_2 \frac{dP_{2\to 4}(t)}{dt} + \pi_3 \frac{dP_{3\to 4}(t)}{dt},$$

where π_i are the equilibrium probabilities of finding the system in state i. We therefore require the transition probabilities $P_{i\to j}(t)$. These transition probabilities obey a similar master equation, which is conveniently written in matrix form as

$$\frac{d\mathbf{P}(t)}{dt} = \mathbf{P}(t)\mathbf{K},$$

where $\mathbf{P}(t)$ is the matrix with elements $P_{i\to j}(t)$ and $\mathbf{K}$ is the matrix of the associated rate constants $k_{i\to j}$. This equation is readily solved by determining the eigenvalues λ and eigenvectors of **K**, so that **P**(t) may be written as

$$\mathbf{P}(t) = \mathbf{A}_1 \exp(\lambda_1 t) + \mathbf{A}_2 \exp(\lambda_2 t) + \mathbf{A}_3 \exp(\lambda_3 t),$$

where $\mathbf{A}_i$ are determined from the eigenvectors of **K**. The appropriate $P_{i\rightarrow j}(t)$ may then be inserted into the equation for $dP_{i\rightarrow 4}(t)/dt$, which are in turn inserted into the equation for $f(t)$. Grouping like exponentials indicates that $\lambda_i = -\kappa_i$ and identifies w_i, allowing for calculation of $k_{\rightarrow \mathrm{high}}$. The same procedure is used for calculating the rate of transition into the 0.1 FRET state. Essentially the same calculation was performed in determining the rates of hybrid and classical state formation, as has been previously described (6).

Structural modeling of observed FRET states. In the structural models constructed here, the nomenclature was chosen to coincide with the solution-state cryo-EM reconstructions. The "closed" state represents the position of the L1 stalk that is closest to the subunit interface and the E site, which has been described in EF-G-bound ribosome structures (20, 21). The "open" state corresponds to the L1 stalk position that predominates when tRNAs are in their classical configuration and the subunits are unratcheted (22–24). The "extended-open" state (25) represents the only position of the L1 stalk that is consistent with multiple smFRET measurements of the tRNA-to-L1 distance and the tRNA-to-EF-G distance for the same complex. Noller and co-workers (23) use other nomenclature chosen to best describe the existing x-ray structures. We note that our extended-open conformation corresponds to the open conformation of Noller and co-workers. Our open conformation corresponds to the closed conformation of Noller and co-workers. Our closed conformation corresponds to the overly closed conformation of Noller and co-workers.

Ribosomal subunits.

The overall structures of the 30S and 50S subunits were based on the high-resolution 70S *E. coli* structure (PDB accession codes 2QAL and 2QAM) (26). To achieve the ratcheted conformation of the 30S subunit, the subunits were docked into cryo-EM reconstructions of the *E. coli* ribosome in the ratcheted state (21) and checked against higher resolution reconstructions of *T. thermophilus* in the ratcheted state (20). In particular, we have aligned the ratcheted 30S subunit and the L1 stalk to the 70S-EF-G (GDPNP) map by using Crystallography and NMR System (CNS)32 by overlap of structure factors. The 30S subunit and L1 stalk were moved as rigid bodies. Protein L27 was homology modeled by using the high-resolution structure of the *T. thermophilus* ribosome (22) (PDB accession code 2J01).

L1 stalk.

The *E. coli* L1 stalk was homology modeled by using the *T. thermophilus* 70S high-resolution structure (23) (PDB accession code 1VS9) with previously described techniques (27). The orientation of the closed conformation of the L1 stalk was achieved by aligning conserved nucleotides in the L1 stalk of *E. coli* with those of *T. thermophilus*. The orientation of the open conformation was determined by docking the *E. coli* L1 stalk into the *T. thermophilus* cryo-EM reconstruction. The 23S rRNA regions of 2091–2092 and 2195–2196 were motif modeled by using previously described techniques (27). The extended open state was constructed by aligning conserved nucleotides near the L1 stalk of the *E. coli* structure with the *D. radiodurans* 50S high-resolution structure (25) (PDB accession code 1LNR). The connecting nucleotides were modeled as described above.

tRNAs.

Classical A/A and P/P tRNA states were based on 70S high-resolution structures and modeled to maintain the tRNA–rRNA interactions. The *E. coli* structure and the *T. thermophilus* structure (PDB accession code 2J01) were used to maintain the observed hydrogen bond interactions between the A- and P-site tRNA anticodon stem loops and the 30S subunit. The *T. thermophilus* A/A tRNA (22) was superimposed on the *E. coli* A-site anticodon stem loop (26). Interactions between the tRNA 3′-CCA ends and the 50S subunit in the A and P sites are critical for the classical state. Because no high-resolution structures of the intact ribosome include interactions of both the A- and P-site 3′-CCA ends, the high-resolution structure with A- and P-site 3′-CCA end analogs was used for these interactions (28) (PDB accession code 1Q86).

Hybrid-state tRNAs were positioned to preserve 30S and 50S hydrogen bonding interactions while achieving the A/P and P/E positions. E-site contacts were based on the *T. thermophilus* E/E state structure (PDB accession code 1VS9). The P/E-tRNA body was docked into cryo-EM reconstructions (20, 21). To maintain ribosome interactions observed in protection studies, while simultaneously maintaining the tRNA fold and helical parameters, two conditions had to be satisfied: (*i*) The 30S subunit must be ratcheted; and (*ii*) the mRNA must be moved by the distance equivalent to approximately 1.5 nucleotides in the 5′ direction (i.e., towards the E site). This model preserves the interactions determined by previous protection studies (29) and x-ray crystallography. The hybrid state interactions require a large movement of the P-site tRNA, consistent with cryo-EM studies (21), but only a small movement of the A-site tRNA. In particular, the A/P-state tRNA was modeled by assuming the 3′-CCA end to be flexible and moving the 3′-CCA end to make the correct 50S P-site hydrogen bond and base pairing interactions (e.g., G2252-C75), while minimally moving the tRNA body.

L7/L12 stalk.

The L7/L12 stalk was constructed by using procedures previously described (30).

Fluorophores.

Cy3 and Cy5 were modeled by using Ghemical (31), according to the structures provided by the manufacturer (GE Healthcare). The Cy3- and Cy5-maleimide fluorophores used to label tRNAs and L1 contain a 6-carbon linker between the fluorophore and the amide bond formed at the thiol group of the s^4U8 or the cysteine residues. The FRET labels have substantial conformational freedom. FRET distance estimates were used to position the FRET labels to simultaneously satisfy two smFRET distance estimates while avoiding any steric crowding (i.e., the L1-tRNA and tRNA-tRNA distances in the case of the A-site tRNA-bound complex and L1-tRNA and EF-G-tRNA distances in the case of the EF-G-bound complex). Interestingly, two simultaneous constraints, combined with the steric constraints of the ribosome itself, left few possibilities to position the Cy3 and Cy5 labels.

tRNA-tRNA distances (Å).

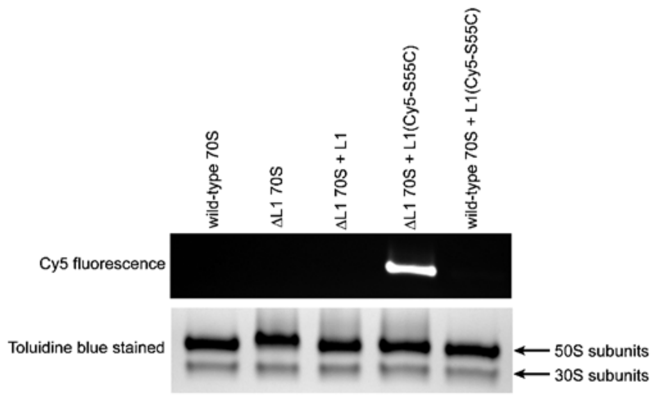

Fig. S1. Composite agarose-acrylamide gel electrophoresis shows specificity of reconstitution of fluorescently labeled L1 with L1-depleted ribosomes. Wild-type and L1-reconsituted ribosomes were prepared as described in *SI Materials and Methods* and run on a composite agarose-acrylamide gel under native conditions (9). Under the current buffer conditions, 70S ribosomes dissociate into 30S and 50S subunits, which run as two distinct bands. (*Top*) Specifically imaging Cy5 fluorescence indicates the presence of the Cy5 fluorophore only in the case of L1-depleted ribosomes reconstituted with L1(S55C-Cy5); wild-type ribosomes incubated with labeled L1 show no indication of nonspecific incorporation. (*Bottom*) The same gel stained with toluidine blue. The ΔL1 70S lane shows a slight upward gel shift owing to the loss of positive charge upon L1 depletion. The gel shift is alleviated upon reconstitution with recombinant L1.

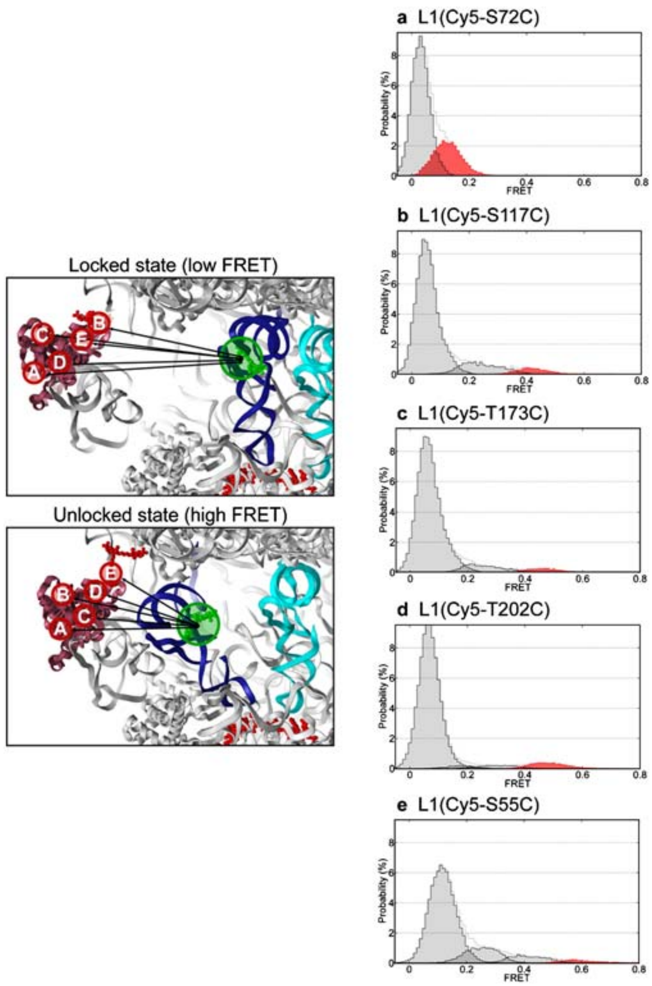

Fig. S2. Ribosome complexes labeled at distinct sites on the L1 protein each display characteristic dynamics and FRET states consistent with structural models. The L1 protein (purple) labeled at the five distinct sites shown (*Left*) exhibited robust incorporation into L1-depleted ribosomes and distributions of FRET states consistent with their estimated distance from Cy3-s^{4}U8-labeled P-site tRNA (blue). (*A*–*E*) Histograms constructed from smFRET trajectories acquired from pre-translocation complexes bearing P-site tRNA^{fMet} and A-site fMet-Phe-tRNA^{Phe}. In all cases, smFRET trajectories were idealized to two-, three-, or four-state Markov chains using the segmental k-means algorithm in QuB (5). Histograms were formed by compiling all the data points assigned to each FRET state during idealization. For each site of labeling, the highest FRET state is highlighted in red to indicate that this state may contain the unlocked ribosome configuration. Consistent with structural models, the S55C labeling position displayed the greatest dynamic range in FRET values allowing for the identification of four distinct FRET states (Fig. S4).

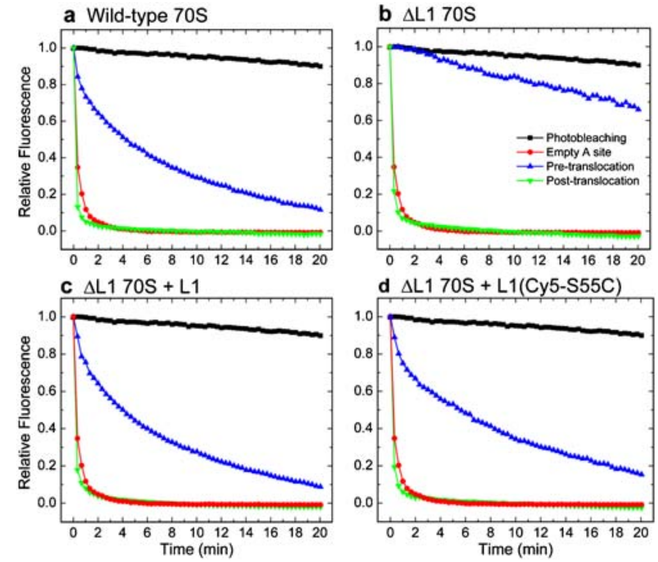

Fig. S3. Puromycin reactivity indicates restoration of function by reconstitution of ΔL1 ribosomes with fluorescently labeled L1. Puromycin (Pmn), an analogue of the 3′ end of tRNA, binds the large subunit PTC, forms a peptide bond, and rapidly dissociates, thus removing the peptide moiety from the ribosome. Pmn reactivity of the ribosome can be detected by acylating the nascent peptide with Cy3 (2, 6). The rate of Pmn reactivity reports on A-site PTC occupancy. When the A site is vacant, Pmn reactivity is rapid. A-site tRNA occupancy in the pretranslocation complex greatly reduces Pmn reactivity owing to occlusion of the Pmn binding site. Residual pretranslocation complex Pmn reactivity reports on the extent of A/P hybrid state formation due to transient vacancy of the Pmn binding site (2, 10, 11). Translocation, which converts pretranslocation complexes to posttranslocation complexes, restores Pmn reactivity. Here, Pmn reactivity experiments performed on (*A*) wild-type (WT), (*B*) L1-depleted (ΔL1), (*C*) L1-reconstituted (ΔL1+L1), and (*D*) L1(Cy5-S55C)-reconstituted ribosomes were used to demonstrate characteristic Pmn reactivities and global translation functions. Pmn reactivity was examined by addition of 2 mM Pmn to surface-immobilized ribosome complexes bearing Cy3-Met-tRNA^{fMet} in the P site (red circles), pretranslocation complexes bearing tRNA^{fMet} in the P site and Cy3-Met-Phe-tRNA^{Phe} in the A site (blue triangles), and posttranslocation complexes bearing tRNA^{fMet} in the E site and Cy3-Met-Phe-tRNA^{Phe} in the P site (green downward triangles). The modest loss of fluorescence due to photobleaching (∼10% over the 20-min observation window, black squares), measured in the absence of Pmn, was well fit by a single exponential process with time constant $\tau = 203$ min. This control was used as a fixed parameter in the fitting in all subsequent experiments. In all systems, Pmn reactivity in the absence of an A-site tRNA (red) was rapid and occurred faster than could be accurately determined at the current time resolution (20 sec). Introduction of tRNA to the A site by enzymatic delivery of EF-Tu(GTP)-Phe-tRNA^{Phe} (1-min incubation), forming pretranslocation complexes, in all systems induced a dramatic decrease in the rate of Pmn reactivity (blue). Pmn-induced fluorescence decay observed in WT pretranslocation complexes (*A*) was well fit by the triple exponential function $A_1 \exp(-t/\tau_1) + A_2 \exp(-t/\tau_2) + A_3 \exp(-t/\tau_3)$, where two dominant time constants in addition to the background photobleaching rate were observed: $\tau_1 = 8.13$ min (73%); $\tau_2 = 0.209$ min (19%). ΔL1 pretranslocation complexes (*B*) reacted more slowly and fit to a single time constant: $\tau = 50.6$ min. This finding is consistent with decreased hybrid state formation (6). ΔL1+L1 pretranslocation complexes (*C*) showed a return to WT behavior where again two dominant time constants in addition to the background photobleaching rate were observed: $\tau_1 = 7.42$ min (78%); $\tau_2 = 0.197$ min (16%). ΔL1+ Cy5-S55C-L1 pretranslocation complexes yielded Pmn reactivity consistent with ∼90% recovery of hybrid state formation over the ΔL1 case (*D*): $\tau_1 = 9.96$ min (74%); $\tau_2 = 0.197$ min (18%). For all pretranslocation complexes (*A*–*D*), 2-min incubation with 10 μM EF-G and 2 mM GTP restored >90% rapid Pmn reactivity consistent with an efficient formation of posttranslocation complexes during the incubation period.

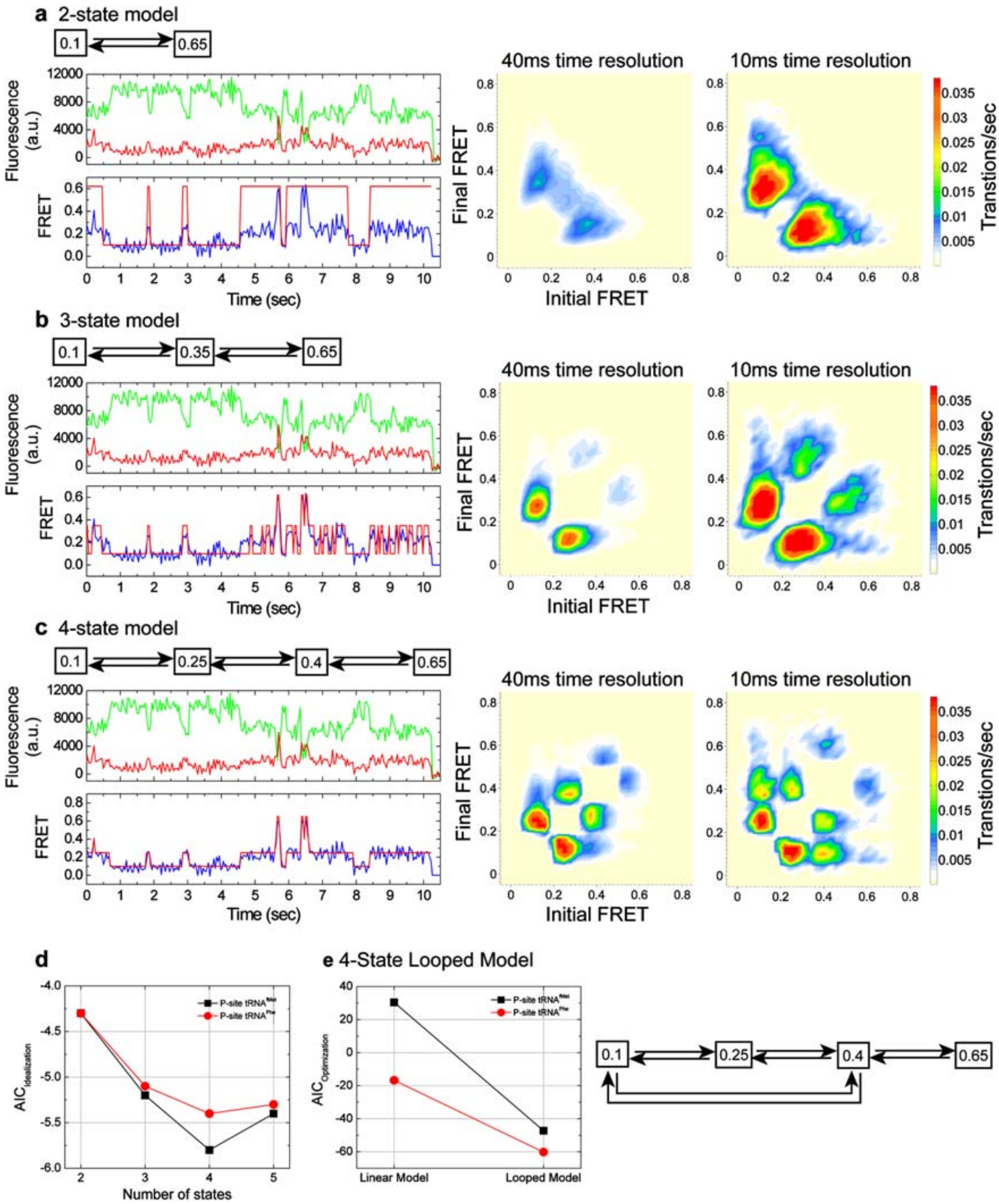

Fig. S4. Multiple models were considered in the kinetic analysis of smFRET trajectories acquired from complexes with labeled L1 and P-site tRNA. (*A*) A smFRET trajectory (Cy3, green; Cy5, red; FRET, blue) shown fit to a model with two states, consistent with the expected FRET values for locked (0.1 FRET) and unlocked (0.65 FRET) conformations. The idealization generated by the segmental k-means algorithm implemented in QuB is overlaid in red (5) and indicates that transitions to intermediate FRET states are not being detected. Transition density plots (TDPs) were formed by measuring the initial and final FRET values for each transition identified by the idealization. TDPs are shown from trajectories acquired at (*Center*) 40- and (*Right*) 10-ms experimental time resolution. At both time resolutions, the broad and asymmetric peaks observed in the TDPs generated by the 2-state model suggest that multiple FRET states have been grouped together. Also, the TDPs suggest that transitions are occurring between 0.1- and ~0.3-FRET states. However, visual inspection of the trajectories indicates that no 0.3-FRET state exists. This discrepancy between the TDPs and the observed FRET transitions is further evidence that multiple FRET states are being averaged during idealization to the 2-state model. (*B*) The same smFRET trajectory is shown fit to a 3-state model, in which a single intermediate FRET state has been included (0.35 FRET). Again, the TDPs obtained at both time resolutions suggest FRET values that differ from those identified by visual inspection of the trajectories, indicating the averaging of multiple FRET states. (*C*) Idealization to a 4-state model indicates adequate representation of the smFRET trajectories. The TDPs generated by the 4-state model show sharp and symmetric peaks corresponding to transitions between the four FRET states. (*D*) To quantitatively assess the idealizations generated from each model considered, the AIC was calculated (12) as described in *SI Materials and Methods.* The idealization of trajectories acquired from complexes with P-site $tRNA^{fMet}$ (black squares) and P-site $tRNA^{Phe}$ (red circles) were both considered during model selection. In both cases, addition of a third and fourth FRET state decreased the AIC, indicating improved fitness. Also in both cases, addition of a fifth state (0.5 FRET) increased the AIC, indicating overfitting of the data. (*E*) The looped four-state model shown was considered during maximum likelihood optimization of the kinetic models in QuB (7). For both complexes considered (black squares, P-site $tRNA^{fMet}$; red circles, P-site $tRNA^{Phe}$), optimization of the looped model resulted in a decrease in the AIC, indicating that the additional connection between the 0.1 and 0.4 FRET states better represents the data.

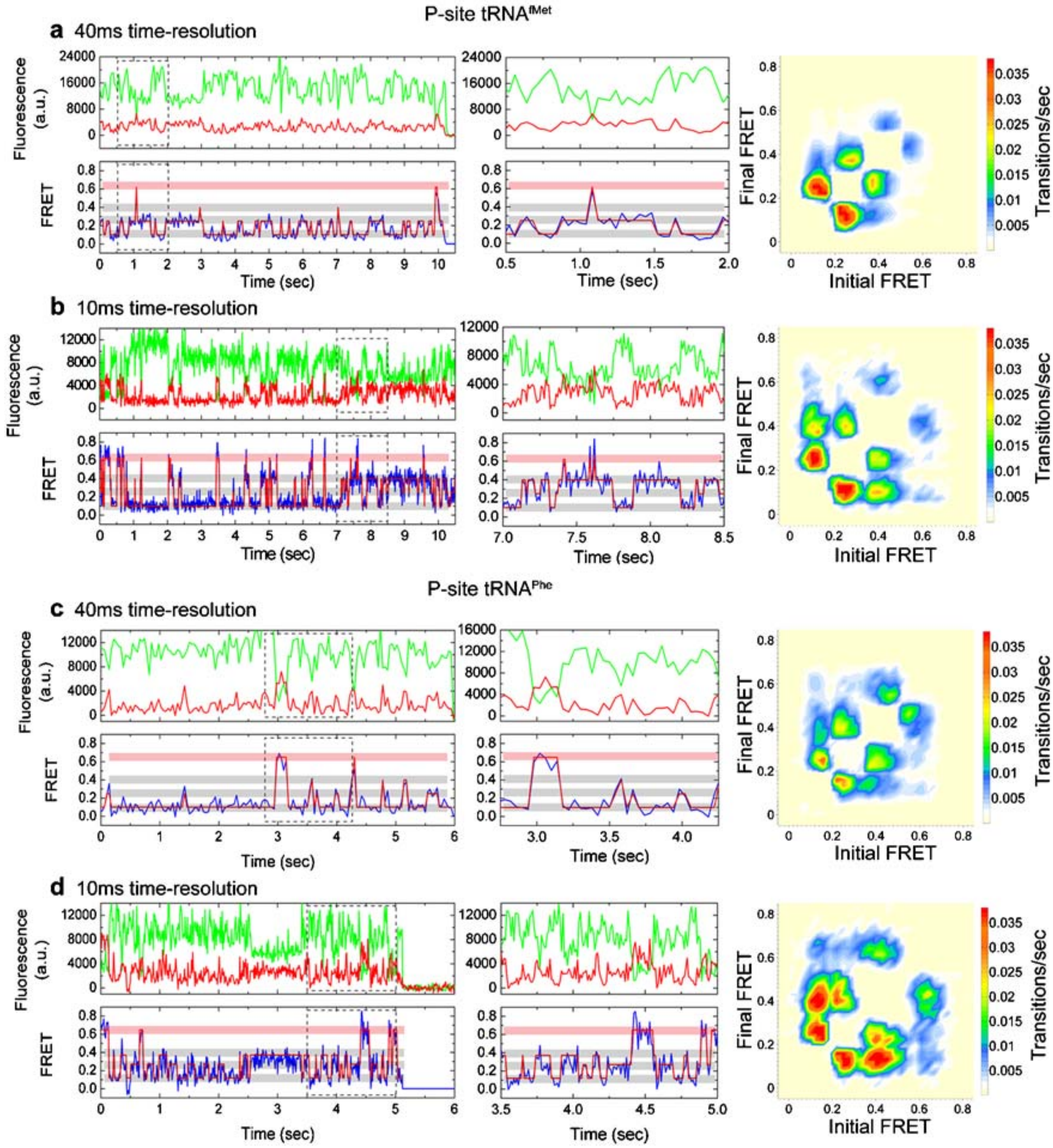

Fig. S5. smFRET trajectories and TDPs from complexes bearing labeled L1 and P-site tRNA indicate the presence of four distinct FRET states. (*A*, *Left*) Single-molecule fluorescence (Cy3, green; Cy5, red) and FRET (blue) trajectories acquired on pretranslocation complexes bearing P-site $\text{tRNA}^{\text{fMet}}$ and A-site fMet-Phe-tRNA^{Phe}. The idealization is overlaid in red on the FRET trace. As indicated, four distinct FRET states are observed in trajectories acquired at 40-ms time resolution. The boxed region is expanded in the center panel. (*A*, *Right*) TDPs indicate the distribution and frequency of transitions determined during idealization of smFRET trajectories. The TDP shows that transitions occur between four FRET states. (*B*) The consideration of a four-state model is supported by smFRET trajectories and TDPs acquired on the same complex at fourfold faster time resolution (10 ms). smFRET trajectories acquired on pretranslocation complexes bearing P-site tRNA^{Phe} and A-site NAc-Phe-Lys-tRNA^{Lys} at (*C*) 40- and (*D*) 10-ms time resolution also show transitions between each of the four FRET states assigned.

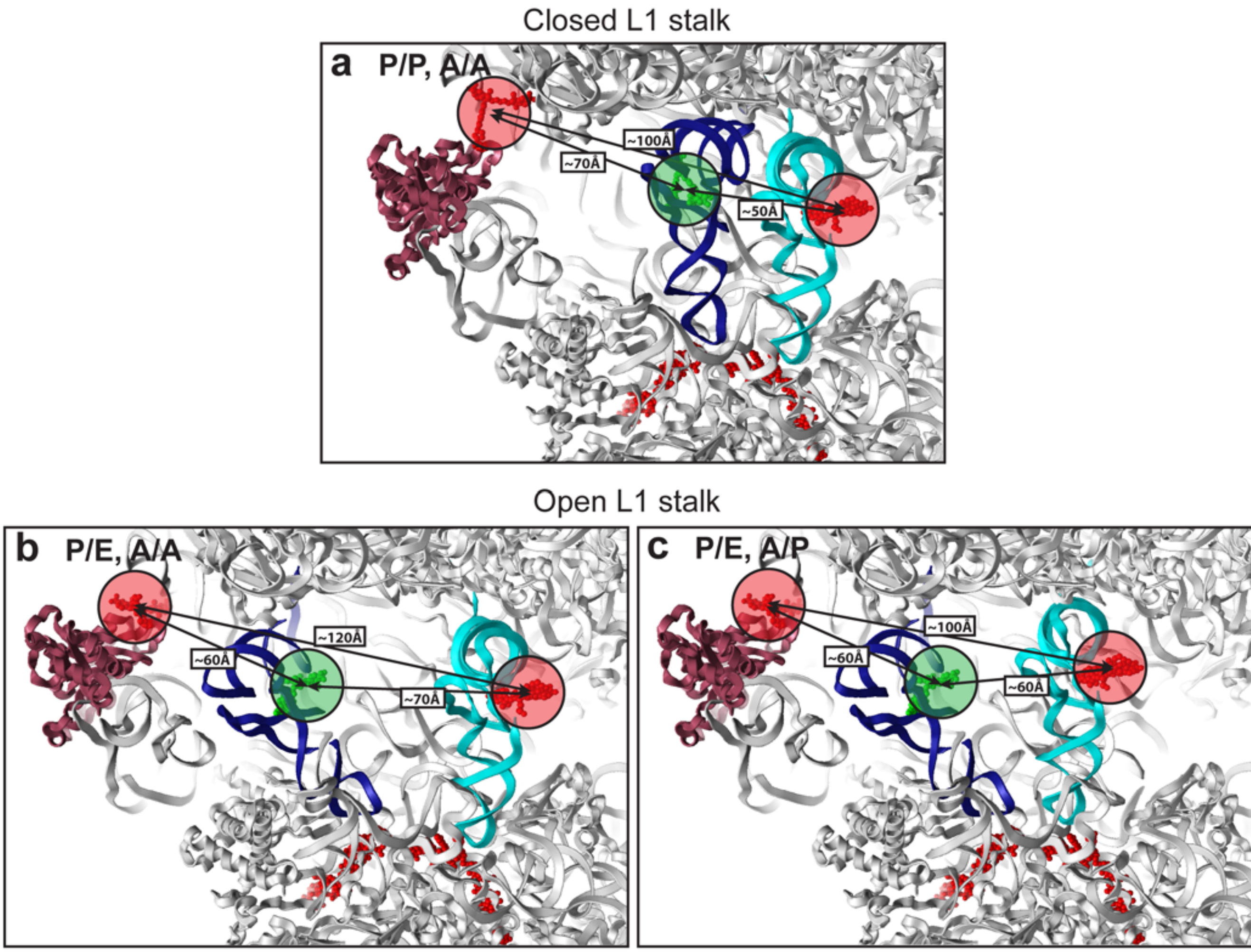

Fig. S6. Atomic models of ribosomes bearing fluorescently labeled tRNAs and L1 protein support the existence of uncoupled motions. Structural models, constructed as described in the *SI Materials and Methods,* show the estimated distances between dyes on A- (cyan) and P-site (blue) tRNAs and the L1 protein (purple) in pretranslocation complexes. (*A*) Both tRNAs are classically bound with the L1 stalk in the closed position, which is consistent with the 0.25-FRET state observed in complexes with labeled L1 and P-site tRNA. (*B*) The P-site tRNA is bound in the P/E hybrid state, whereas the A-site tRNA remains classically bound (hybrid state 2; P/E, A/A), and the L1 stalk is open. (*C*) P- and A-site tRNAs adopt the P/E and A/P hybrid states, respectively (hybrid state-1; P/E, A/P). Either hybrid-state 1 or 2, with the L1 stalk open, could explain the existence of the 0.4-FRET state observed in complexes with labeled L1 and P-site tRNA. The estimated distances between donor and acceptor fluorophores, calculated from structural models and observed FRET values, are taken from Tables S3 and S4.

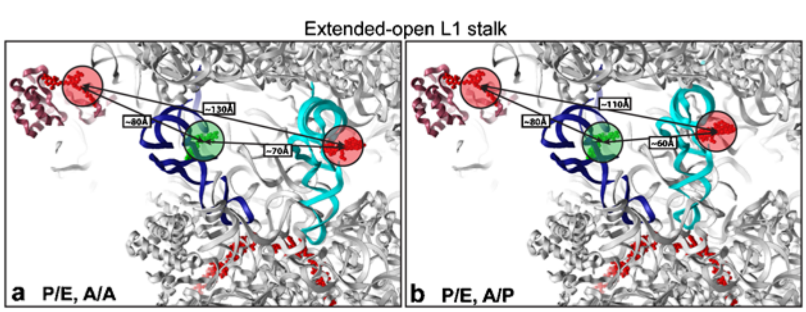

Fig. S7. Atomic models of the ribosome bearing fluorescently labeled tRNAs and L1 protein with the "extended-open" L1 configuration. Structural models, constructed as described in the *SI Materials and Methods,* show the estimated distances between dyes on A- (cyan) and P-site (blue) tRNAs and the L1 protein (purple) in pretranslocation complexes in which the L1 stalk occupies an extended-open configuration. (*A*) P-site tRNA adopts the P/E hybrid state whereas the A-site tRNA remains classically bound (hybrid state-2; P/E, A/A); (*B*) both P- and A-site tRNAs occupy hybrid states (hybrid state-1; P/E, A/P). The estimated distances between donor and acceptor fluorophores, calculated from structural models and observed FRET values, are taken from Table S2.

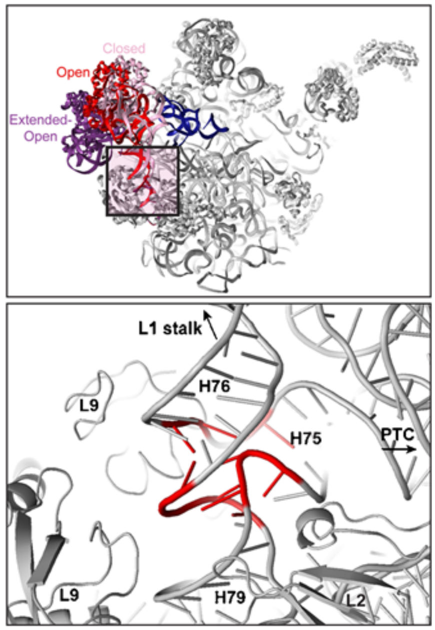

Fig. S8. The L1 stalk may pivot about a conserved hinge region in domain V of 23S rRNA. (*Upper*) Structural model of the *E. coli* 70S ribosome showing three distinct L1 stalk positions, as supported by smFRET observations: extended-open (purple), open (red), and closed (pink). Motions of the L1 stalk domain, comprising 23S rRNA helices H76, H77, and H78, lead to changes in the L1 protein's position relative to P-site tRNA (blue), shown here in a hybrid (P/E) configuration. (*Lower*) L1 stalk motions can be modeled by a pivot-like motion centered on the hinge region formed by the junction of helices H75, H76, and H79. Highly conserved (>98% in bacteria) residues in this region, comprising nucleotides 2085–2099, 2189–2202, and 2221–2231 (*E. coli* numbering), are shown in red (13).

Table S1. Bulk translocation rates

Ribosome	A site	P site	Rate (sec^{-1})
$tRNA^{fMet}$-bound complex			
Wild-type	fMetPhe-$tRNA^{Phe}$	$tRNA^{fMet}$	1.3 ± 0.1
Wild-type*	fMetPhe-$tRNA^{Phe}$	$tRNA^{fMet}$	2.7 ± 0.3
Wild-type, no EF-G	fMetPhe-$tRNA^{Phe}$	$tRNA^{fMet}$	ND
ΔL1	fMetPhe-$tRNA^{Phe}$	$tRNA^{fMet}$	0.40 ± 0.05
ΔL1+L1	fMetPhe-$tRNA^{Phe}$	$tRNA^{fMet}$	1.0 ± 0.2
ΔL1+L1(Cy5-S55C)	fMetPhe-$tRNA^{Phe}$	$tRNA^{fMet}$(Cy3-s^4U8)	0.90 ± 0.1
$tRNA^{Phe}$-bound complex			
Wild-type	NAcPheLys-$tRNA^{Lys}$	$tRNA^{Phe}$	2.0 ± 0.3
Wild-type*	NAcPheLys-$tRNA^{Lys}$	$tRNA^{Phe}$	3.7 ± 0.1
Wild-type, no EF-G	NAcPheLys-$tRNA^{Lys}$	$tRNA^{Phe}$	ND
ΔL1	NAcPheLys-$tRNA^{Lys}$	$tRNA^{Phe}$	0.71 ± 0.01
ΔL1+L1	NAcPheLys-$tRNA^{Lys}$	$tRNA^{Phe}$	1.4 ± 0.1
ΔL1+L1(Cy5-S55C)	NAcPheLys-$tRNA^{Lys}$	$tRNA^{Phe}$(Cy3-s^4U8)	1.3 ± 0.1

Table S2. Kinetic analysis of smFRET trajectories obtained from distinct pretranslocation ribosome complexes

	L1-tRNA FRET transition rates (sec^{-1})								tRNA-tRNA FRET transition rates					
P-site tRNA	$k_{0.1\rightarrow0.25}$	$k_{0.1\rightarrow0.4}$	$k_{0.25\rightarrow0.1}$	$k_{0.25\rightarrow0.4}$	$k_{0.4\rightarrow0.1}$	$k_{0.4\rightarrow0.25}$	$k_{0.4\rightarrow0.65}$	$k_{0.65\rightarrow0.4}$	$k_{0.54\rightarrow0.4}$	$k_{0.54\rightarrow0.25}$	$k_{0.4\rightarrow0.54}$	$k_{0.4\rightarrow0.25}$	$k_{0.25\rightarrow0.54}$	$k_{0.25\rightarrow0.4}$
$tRNA^{fMet}$	0.94 ± 0.09	0.25 ± 0.06	7.3 ± 0.3	5.8 ± 0.4	12 ± 1	18 ± 1	5.8 ± 0.4	23 ± 1	1.3 ± 0.1	1.5 ± 0.1	4.9 ± 0.2	3.8 ± 0.3	5.6 ± 0.3	2.4 ± 0.1
$tRNA^{Phe}$	1.2 ± 0.2	1.1 ± 0.2	13 ± 1	11 ± 1	19 ± 1	14 ± 1	9.1 ± 0.7	17 ± 1	1.7 ± 0.1	2.1 ± 0.2	3.0 ± 0.8	4.0 ± 0.2	2.1 ± 0.3	1.2 ± 0.2

Table S3. Structural modeling of the ribosome with fluorescently labeled L1 and tRNA predict interdye distances that are in excellent agreement with the experimentally observed FRET values

tRNA	30S subunit	L1 stalk	FRET	Experimental	Model
P/P	Unratcheted	Extended open	<0.1	ND	~100
P/P	Unratcheted	Open	0.1	~80	~80
P/P	Unratcheted	Closed	0.25	~70	~70
P/E	Ratcheted	Extended open	0.1	~80	~80
P/E	Ratcheted	Open	0.4	~60	~60
P/E	Ratcheted	Closed	0.65	~50	~50
A/A	Unratcheted	Extended open	<0.03	ND	~130*
A/A	Unratcheted	Open	~0.03	ND	~120*
A/A	Unratcheted	Closed	ND	ND	~100*
A/P	Ratcheted	Extended open	ND	ND	~110*
A/P	Ratcheted	Open	ND	ND	~100*
A/P	Ratcheted	Closed	0.5	ND	~90*

Table S4. Structural modeling of the ribosome with fluorescently labeled L1 and tRNA predict inter-dye distances that are in excellent agreement with the experimentally observed FRET values

		FRET	Experimental	Model
P/P	A/A	0.54	~55	~50
P/E	A/A	0.25	~70	~70
P/E	A/P	0.4	~60	~60

The "model" distances presented are estimates determined from the structural models shown in Fig. 1 and Figs. S5–S7, which were generated from high-resolution crystal structures (resolution <3.5 Å) and cryo-EM reconstructions (resolution 7–10 Å) as described in *SI Materials and Methods*. Here, dyes were placed at the site of labeling into the modeled structures. The dye center of mass, approximated by the conjugated polyene core of the molecule, was estimated through energy minimization. The experimental interdye distances were estimated from FRET measurements where R_0 was shown to be ~56 Å by using control Cy3/Cy5-labeled oligonucleotides of known length. No correction was made for differences in detection efficiency or quantum yields of the two fluorophores (8) (i.e., $\gamma = 1$). As previously reported, three structural configurations have been putatively assigned to the observed FRET states observed on complexes bearing labeled A- and P-site tRNAs (6). In all cases the experimentally estimated distances ("experimental") are in excellent agreement with the distances predicted by the atomic models ("model"). Configurations not determined are noted with "ND." Modeled distances have an estimated error of ±5 Å.

1. Studer SM, Feinberg JS, Joseph S (2003) Rapid kinetic analysis of EF-G-dependent mRNA translocation in the ribosome. *J Mol Biol* 327:369–381.
2. Blanchard SC, Kim HD, Gonzalez RL, Jr, Puglisi JD, Chu S (2004) tRNA dynamics on the ribosome during translation. *Proc Natl Acad Sci USA* 101:12893–12898.
3. Walker SE, Shoji S, Pan D, Cooperman BS, Fredrick K (2008) Role of hybrid tRNA-binding states in ribosomal translocation. *Proc Natl Acad Sci USA* 105:9192–9197.
4. Peske F, Savelsbergh A, Katunin VI, Rodnina MV, Wintermeyer W (2004) Conformational changes of the small ribosomal subunit during elongation factor G-dependent tRNA-mRNA translocation. *J Mol Biol* 343:1183–1194.
5. Qin F (2004) Restoration of single-channel currents using the segmental k-means method based on hidden Markov modeling. *Biophys J* 86:1488–1501.
6. Munro JB, Altman RB, O'Connor N, Blanchard SC (2007) Identification of two distinct hybrid state intermediates on the ribosome. *Mol Cell* 25:505–517.
7. Qin F, Auerbach A, Sachs F (1996) Estimating single-channel kinetic parameters from idealized patch-clamp data containing missed events. *Biophys J* 70:264–280.
8. Michalet X, Weiss S, Jager M (2006) Single-molecule fluorescence studies of protein folding and conformational dynamics. *Chem Rev* 106:1785–1813.
9. Dahlberg AE, Dingman CW, Peacock AC (1969) Electrophoretic characterization of bacterial polyribosomes in agarose-acrylamide composite gels. *J Mol Biol* 41:139–147.
10. Semenkov Y, Shapkina T, Makhno V, Kirillov S (1992) Puromycin reaction for the A site-bound peptidyl-tRNA. *FEBS Lett* 296:207–210.
11. Sharma D, Southworth DR, Green R (2004) EF-G-independent reactivity of a pre-translocation-state ribosome complex with the aminoacyl tRNA substrate puromycin supports an intermediate (hybrid) state of tRNA binding. *RNA* 10:102–113.
12. Akaike H (1974) A new look at statistical model identification. *IEEE Trans Automat Contr* 19:716–723.
13. Cannone J, et al. (2002) The comparative RNA web (CRW) site: An online database of comparative sequence and structure information for ribosomal, intron, and other RNAs. *BMC Bioinformatics* 3:2–32
14. Munro JB, Altman RB, Tung CS, Sanbonmatsu KY, Blanchard SC (2009) A fast dynamic mode of the EF-G-bound ribosome. *EMBO J*, in press. Please refer questions to Hartmut Vodermaier, PhD Editor The EMBO Journal h.vodermaier@embojournal.org
15. Blanchard SC, Gonzalez RL, Kim HD, Chu S, Puglisi JD (2004) tRNA selection and kinetic proofreading in translation. *Nat Struct Mol Biol* 11:1008–1014.
16. McKinney SA, Joo C, Ha T (2006) Analysis of single-molecule FRET trajectories using hidden Markov modeling. *Biophys J* 91:1941–1951.
17. McQuarrie ADR, Tsai CL (1998) *Regression and Time Series Model Selection* (World Scientific, Hackensack, NJ).
18. Qin F, Auerbach A, Sachs F (1997) Maximum likelihood estimation of aggregated Markov processes. *Proc Biol Sci* 264:375–383.
19. Colquhoun D, Hawkes AG (1981) On the stochastic properties of single ion channels. *Proc R Soc Lond B* 211:205–235.
20. Connell SR, et al. (2007) Structural basis for interaction of the ribosome with the switch regions of GTP-bound elongation factors. *Mol Cell* 25:751–764.
21. Valle M, et al. (2003) Locking and unlocking of ribosomal motions. *Cell* 114:123–134.
22. Selmer M, et al. (2006) Structure of the 70S ribosome complexed with mRNA and tRNA. *Science* 313:1935–1942.
23. Korostelev A, Ermolenko DN, Noller HF (2008) Structural dynamics of the ribosome. *Curr Opin Struct Biol* 12:674–683.
24. Schuette JC, et al. (2009) GTPase activation of elongation factor EF-Tu by the ribosome during decoding. *EMBO J* 28:755–765.
25. Harms J, et al. (2001) High resolution structure of the large ribosomal subunit from a mesophilic eubacterium. *Cell* 107:679–688.

26. Borovinskaya MA, Shoji S, Holton JM, Fredrick K, Cate JHD (2007) A steric block in translation caused by the antibiotic spectinomycin. *ACS Chem Biol* 2:545–552.
27. Tung C, Joseph S, Sanbonmatsu K (2002) All-atom homology model of the Escherichia coli 30S ribosomal subunit. *Nat Struct Biol* 9:750–755.
28. Hansen JL, Schmeing TM, Moore PB, Steitz TA (2002) Structural insights into peptide bond formation. *Proc Natl Acad Sci USA* 99:11670–11675.
29. Moazed D, Noller HF (1989) Intermediate states in the movement of transfer RNA in the ribosome. *Nature* 342:142–148.
30. Diaconu M, et al. (2005) Structural basis for the function of the ribosomal L7/12 stalk in factor binding and GTPase activation. *Cell* 121:991–1004.
31. Hassinen T, Peräkylä M (2001) New energy terms for reduced protein models implemented in an off-lattice force field. *J Comput Chem* 22:1229–1242.
32. Brünger AT, Adams PD, Clore GM, DeLano WL, Gros P, Grosse-Kunstleve RW, Jiang JS, Kuszewski J, Nilges M, Pannu NS, Read RJ, Rice LM, Simonson T, Warren GL. (1998) Crystallography & NMR system: A new software suite for macromolecular structure determination *Acta Crystallogr D Biol Crystallogr* 54:905-21.